POLYPUBLIE
Polytechnique Montréal

POLYTECHNIQUE MONTRÉAL
UNIVERSITÉ D'INGÉNIERIE

Titre: Multiscale characterization of the fracture mechanics of additively manufactured short fiber-reinforced composites
Title:

Auteurs: Alessandra Lingua, Facundo Sosa-Rey, Sébastien Pautard, Daniel Therriault, & Martin Lévesque
Authors:

Date: 2023

Type: Article de revue / Article

Référence: Lingua, A., Sosa-Rey, F., Pautard, S., Therriault, D., & Lévesque, M. (2023). Multiscale characterization of the fracture mechanics of additively manufactured short fiber-reinforced composites. Engineering Fracture Mechanics, 289, 109343 (19 pages). https://doi.org/10.1016/j.engfracmech.2023.109343
Citation:

Document en libre accès dans PolyPublie
Open Access document in PolyPublie

URL de PolyPublie: https://publications.polymtl.ca/54585/
PolyPublie URL:

Version: Version finale avant publication / Accepted version
Révisé par les pairs / Refereed

Conditions d'utilisation: Creative Commons Attribution-Utilisation non commerciale-Pas d'oeuvre dérivée 4.0 International / Creative Commons Attribution-NonCommercial-NoDerivatives 4.0 International (CC BY-NC-ND)
Terms of Use:

Document publié chez l'éditeur officiel
Document issued by the official publisher

Titre de la revue: Engineering Fracture Mechanics (vol. 289)
Journal Title:

Maison d'édition: Elsevier
Publisher:

URL officiel: https://doi.org/10.1016/j.engfracmech.2023.109343
Official URL:

Mention légale:
Legal notice:

Ce fichier a été téléchargé à partir de PolyPublie, le dépôt institutionnel de Polytechnique Montréal
This file has been downloaded from PolyPublie, the institutional repository of Polytechnique Montréal

https://publications.polymtl.ca

Multiscale characterization of the fracture mechanics of additively manufactured short fiber-reinforced composites

Alessandra Lingua[a], Facundo Sosa-Rey[a], Sébastien Pautard[b], Daniel Therriault[a], Martin Lévesque[a,*]

[a] *Laboratory for Multiscale Mechanics, Department of Mechanical Engineering, Polytechnique Montreal, 2900 boul. Edouard-Montpetit, Montreal, QC, Canada*
[b] *Safran Composites, Safran Group, 33 Avenue de la Gare, Itteville 91760, France*

Abstract

We present a multiscale characterization approach to experimentally investigate the influence of architectural features, namely pores, weakly bonded filaments' interfaces, and layer stacking, on the failure of composites manufactured by fused filament fabrication. Combining standard approaches, such as tensile and flexural tests, with contactless techniques, we identified the local phenomena driving the damage of 3D-printed short carbon fiber-reinforced polyetheretherketone specimens. The elastic and fracture tests highlighted the process-induced anisotropy and the incomplete interface adhesion resulting in the transverse tensile modulus drop to around 20% of the longitudinal value. Equivalent fracture toughness was measured for a crack propagation along filaments' and layers' interfaces, while the stress intensity factors doubled for a crack propagation involving the filaments' breakage, when compared to the interface failure. The displacement and strain contours obtained by digital image correlation emphasize the influence of the stacking (*i.e.*, $0° - 90°$, $\pm\ 45°$) on the preferential crack propagation at the layers' and filaments' interfaces. The specimen inspection by scanning electron microscopy and by X-ray tomography further highlighted the influence of the printed composites' meso and microscale architecture on the fracture mechanisms, such as the simultaneous damage of parallel $\pm\ 45°$ oriented layers' interfaces or the *zig-zag* crack propagation for specimens with $\pm\ 45°$ stacking undergoing intralayer delamination. The elastic and fracture properties, together with the full-field measurements, provide the tools to guide the design of complex and reliable components for high-performance applications (*e.g.*, aerospace, automotive) and benchmark for damage prediction models.

Keywords: Fused filament fabrication, Short fiber-reinforced composites, Fracture mechanics, Digital image correlation, Computed tomography

Nomenclature

ν Poisson's ratio

*Corresponding author
Email address: martin.levesque@polymtl.ca (Martin Lévesque)

σ	Stress
θ	Standard deviation confidence
ε	Strain
ε_{yy}	Vertical lagrangian strain
a_0	Pre-crack length
B	SENB specimen thickness
E_l	In-plane longitudinal modulus of elasticity
E_t	In-plane transverse modulus of elasticity
K_{IC}	Stress intensity factor
P	Applied load
P_{max}	Peak load
S	Bending fixture cylinders gap
V	Vertical displacement
W	SENB specimen width
CF	Carbon fiber
CT	Compact tension
DIC	Digital image correlation
FFF	Fused filament fabrication
PEEK	Polyetheretherketone
ROI	Region of interest
SEM	Scanning electron microscopy
SENB	Single edge notch bending

1. Introduction

The combination of fused filament fabrication (FFF) and composites enables the manufacturing of lightweight structures with enhanced strength and stiffness, when compared to their pure resins [1, 2, 3]. The extrusion-based manufacturing of components for high-performance applications involves the ad-hoc development of composite filaments and the optimization of the process window to minimize manufacturing defects [4, 5]. One approach consists in embedding short fibers within the polymeric matrix before feeding the printer nozzle to maximize the fibers' impregnation and hinder their pull-out under load [6, 7]. Even if the deposition of continuous fibers maximizes the strength and stiffness in the reinforcement direction, the process involves challenges such as the fibers impregnation, the matrix and reinforcement controlled distribution, and interlayer bonding [8, 9].

FFF involves depositing filaments layer-wise on the heated printing platform under a controlled temperature environment. The deposition of a circular section composite filament often results in the formation of interfilament porosity, expanded by shrinking during consolidation, and intrafilament porosity at the fiber-matrix level [10, 11]. Moreover, the sudden material cooling from the extrusion to the chamber temperature hinders the interfacial molecular diffusion and entanglement, promoting the part warping and interlayer delamination under operating conditions [12, 13]. The incomplete layers' and filaments' adhesion is more pronounced for high-performance semi-crystalline reinforced polymers, such as polyetheretherketone (PEEK), when compared to polylactic acid (PLA) and acrylonitrile butadiene styrene (ABS) due to the high processing temperatures and specific cooling rates required for their proper consolidation [14, 15, 16, 17]. The fibers' directional deposition during extrusion delivers orthotropic parts likely to fail prematurely under Mode I load [18, 19]. Such multiscale architectural features (e.g., porosity, weak interfaces, partial fiber-matrix adhesion) determine the damage nucleation and propagation and drive the fracture mechanics of FFF composites [20].

Researchers mainly focused on identifying the optimal processing window and toolpath maximizing the strength, stiffness, and structural toughness of FFF composites through standardized testing [21, 22, 23]. However, recent works highlighted the potential of multiscale, contactless characterization approaches, such as scanning electron microscopy (SEM), X-ray tomography, and digital image correlation (DIC), to investigate the architecture-based crack propagation in composites made by FFF [5, 24, 25]. Moreover, the availability of multiscale full-field measurements promotes the development of models reproducing the damage nucleation and propagation due to the presence of material and manufacturing defects, and architectural features (*e.g.*, layer stacking, multiscale porosity). Indeed, such data sets can be used by researchers attempting to model the fracture in such materials to either feed or validate the predictions [26]. Yavas et al. studied the strain distribution and the process zone size at the crack tip of composite compact tension specimens by DIC to understand the interlayer and cross-layer fracture mechanisms [27, 28]. However, the measurements scale of tens of millimeters primarily allows for only estimating the fracture process zone size and shape and extracting maximum strain values [29]. Yu et al. proposed an in-situ X-ray tomography-based characterization approach to investigate the three-dimensional fracture

behavior of polylactic acid composites [25]. The authors monitored the different 3D cracking mechanisms under tensile loading for specimens with distinct stackings and correlated them with the stress-strain curves, highlighting the need for multiscale characterization to describe failure exhaustively.

To the best of our knowledge, no multiscale characterization approach describing the 3D printed composites' elastic and fracture behavior, their mesoscale damage mechanisms, and the effect of 3D fibers and pores dispersion on their fracture mechanics is available in the literature.

This work presents a multiscale characterization of the mechanical behavior of specimens manufactured with short carbon fiber-reinforced PEEK, suitable for aerospace applications due to its relatively high strength and stiffness, and temperature and chemical resistance [30]. We tested specimens with different stacking sequences, namely 0°, $0° - 90°$, 90°, and $\pm 45°$, thus involving different damage propagation dynamics. We first characterized the material's elastic and fracture properties through standard tensile and three-point bending ASTM tests. We then identified the different interface local damage propagation mechanisms by studying the full displacement and strain measurements by microstereoscopic DIC, allowing for the damage tracking over a region of interest of $\sim 4 \times 2.5$ mm^2 at the crack tip. We focused on the interlayer and intralayer delamination, the most severe failure mechanisms under load for FFF composites due to the incomplete necking at the filaments' interface [31, 32, 33]. We validated the observation drawn from the DIC measurements by inspecting the specimens' cross-section and fracture surface by SEM and the 3D fibers and pores arrangement by X-ray tomography. The outcomes of this work suggest a generalized approach to characterize the multiscale failure of composites manufactured by FFF while providing the mechanical properties and full-field measurements to develop and validate constitutive models to reproduce their damage.

2. Material and methods

2.1. Specimens manufacturing and preparation

We manufactured specimens for the elastic and fracture properties characterization using the AON3D M2 printer with a Dyze Design DyzeXtruder Pro installed and 30 w% short carbon fiber (CF)-reinforced TECAFIL victrex® PEEK supplied by Ensinger due to its relatively high nominal strength [34]. Prior to printing, we stored the spools in a vacuum environment at 60°C and we dried them at 120°C for at least 1 hour. We identified the set of printing parameters listed in Table 1 based on the supplier's technical specifications, aiming to minimize the interfilament porosity. As a result, a nozzle diameter of 0.4 mm and a temperature of 440°C delivered specimens whose dimensions agreed with the standard design tolerances without any nozzle clogging during manufacturing. We set the AON3D polyetherimide bed and chamber temperatures at their maximum values, 180°C and 120°C, respectively, to promote molecular diffusion and thus the adhesion at the filaments' and layers' interfaces. We defined the specimen stacking and printing approach in the GCode for the manufacturing of one specimen per process for the sake of consistency.

Figure 1 illustrates the specimens geometry, printing strategy, and reference stacking orientations (0° and 90°) defined to characterize the anisotropic elastic and fracture behavior of CF-reinforced PEEK made by FFF. We followed two printing strategies to characterize the in-plane and out-of-plane mechanical properties of ($\bar{x}\bar{y}$) and ($\bar{z}$) specimens, respectively. We focused exclusively on the in-plane elastic properties, neglecting the out-of-plane elastic properties, which are considerably lower than the in-plane properties [27]. We manufactured four standard Type IV dogbone specimens for each stacking, namely 0°, 90°, and $0° - 90°$, for the derivation of the in-plane longitudinal and transverse elastic properties. We measured the extension under loading with an MTS uniaxial extensometer (model 634_25F-25). Since the biaxial extensometer had a gauge length of 50 mm, it was necessary to print a set of $\bar{x}\bar{y}$ Type I dogbones for the measurement of the Poisson's ratios.

Figure 1a shows the standard single edge notched bending (SENB) specimens designed to characterize the interlayer ($\bar{z}$ specimen) and intralayer ($\bar{x}\bar{y}$ specimen) fracture properties, involving the crack propagation between FFF layers or between and across filaments within the same deposited layer.

The main advantage of the SENB configuration is its geometrical simplicity and reduced post-processing required, with minimum material waste (the notch is not printed but manually carved after manufacturing), when compared to the compact tension geometry. We manufactured four specimens for each printing strategies ensuring the straight crack propagation, namely 0°, 90°, and $0° - 90°$, to evaluate the influence of the fibers' alignment on the specimens' fracture toughness. We carved a 5 mm notch with a Buehler Isomet low-speed saw, successively sharpened using a Stanley razor blade, to achieve the stress concentration at the crack tip that ensures plane strain, according to the ASTM D5045 standard [35].

Figure 1b shows the miniature compact tension (CT) specimens design, defined for the characterization of the local interface damage and failure mechanisms under opening mode delamination by microsteresoscopic DIC. We selected the CT configuration for the characterization of the local failure mechanisms by DIC due to the stable specimen's alignment in the grips under opening load, when compared to the bending framework. We manufactured four $\bar{z}$ and four $\bar{x}\bar{y}$ CT specimens with $0° - 90°$ and $\pm 45°$ plies to study the mesoscale interlayer and intralayer crack propagation of specimens with a low degree of anisotropy, interesting for structural applications.

We pre-cracked the $\bar{x}\bar{y}$ CT specimens with the custom-made pendulum system described in Appendix C, controlling the impact force transferred to the blade and thus the crack length. The pendulum framework minimum impact force was above the pre-cracking threshold necessary to sharpen the notch on the $\bar{z}$ CT specimens midplane, thus pre-cracked with

Table 1: FFF printing parameters for the manufacturing of short fibers reinforced dogbone, SENB, and CT specimens for the multiscale characterization of the elastic, fracture and local properties of FFF CF reinforced PEEK.

Nozzle diameter [mm]	**Temperature [°C]**			**Speed [mm/s]**	**Layer height [mm]**	**Extrusion width [mm]**
	Nozzle	Bed	Chamber			
0.4	440	180	120	35	0.2	0.42

a conventional hammer and razor blade. The image correlation required the specimens' polishing using the Buehler Metaserv 2000 grinder-polisher with CarbiMet™ silicon carbide abrasive paper of decreasing grit sizes of 100, 240, and 320. We then applied two layers of Rust-Oleum mat white paint and nebulized carbon black ink with an Abest airbrush on the dried paint until we obtained a fine random speckle pattern over the specimen's surface.

2.2. Mechanical characterization

2.2.1. Macroscale characterization

2.2.1.1 Tensile test

We loaded the Type I and Type IV specimens using the Insight electromechanical testing machine with a 50 kN load cell installed at a 5 mm/min testing rate (crosshead displacement control). The rough grips installed on the mechanical testing machine prevented the specimens' slippage while maintaining their alignment during loading. We measured the specimens' narrow section elongation along the x and y directions using the MTS axial (gauge length = 25 mm) and biaxial (gauge length = 50 mm) extensometers on Type IV and Type I dogbones, respectively. We derived the specimens' longitudinal and transverse

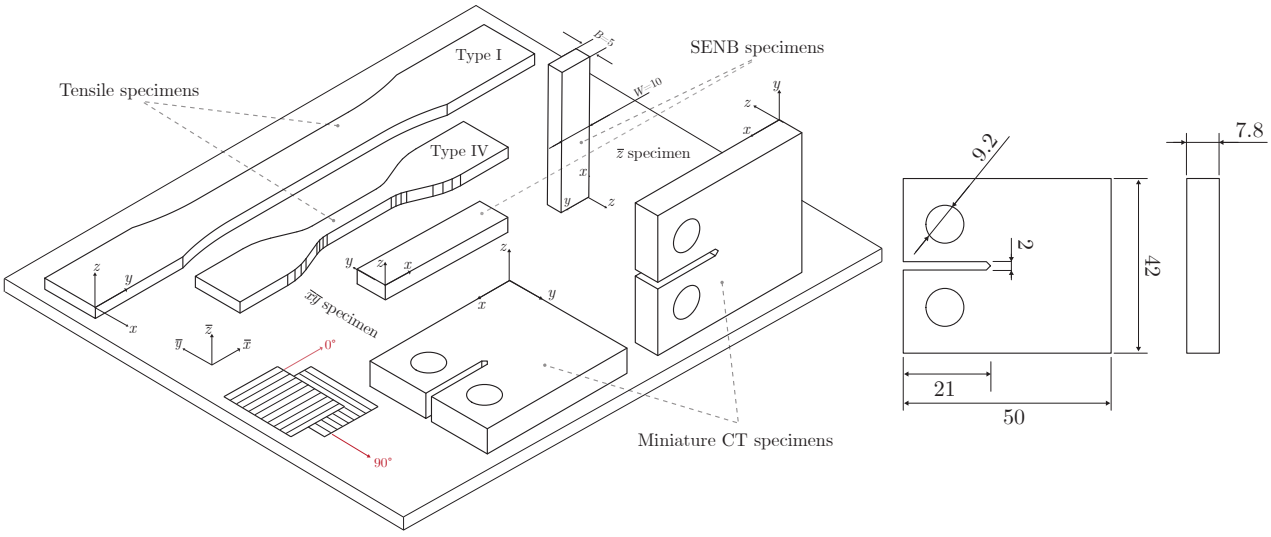

(a) (b)

Figure 1: Specimens designs and printing strategy for investigating the elastic and fracture behavior of 3D printed CF-reinforced PEEK coupons. (a) Type I and Type IV dogbones for the estimation of the elastic properties, SENB specimens, and miniature CT specimens as printed for the characterization of the interlayer ($\bar{z}$) and intralayer ($\bar{x}\bar{y}$) fracture toughness and failure mechanisms of specimens with different stackings. (b) Miniature CT specimens geometry to study the local interlayer and intralayer delamination mechanisms by microstereoscopic DIC. The dimensions are in millimeters. We report the printing reference system ($\bar{x}\bar{y}\bar{z}$) and the characterization reference system (x,y,z), integral with each specimen and configuration and defined for an applied load P along y.

stiffness and ultimate strength from the stress-strain curves by normalizing the elongation with the gauge length and the load with the area measured prior to the test, following the ASTM D638-14 standard [36]. We computed the in-plane longitudinal and transverse modulus of elasticity (E_l, E_t) as the slope of the first degree polynomial fitting of the stress (σ)-strain (ε) curve in the linear domain. The end of the linear domain is defined by a relative error between the first-degree polynomial fitting and the recorded σ-ε curve equal to 0.01. We computed the Poisson's ratio (ν) as the ratio between the transverse and axial strains recorded by the biaxial extensometer at the end of the linear domain previously identified.

2.2.1.2 Three-point bending test

Figure 2 shows the MTS three-point bending fixture designed to transfer the Mode I load from the cylindrical pins to the specimen's notch for straight crack propagation. We installed the testing fixture in an Instron 1365 electromechanical frame with an MTS ReNew controller and a 5 kN load cell capacity for the SENB specimens loading under crosshead displacement control. The grips adapters allowed the load transfer from the machine to the 5 mm diameter fixture cylinders traveling at a crosshead speed of 10 mm/min (0.167 mm/s).

We evaluated the interlayer and intralayer fracture toughness of the SENB specimens with different stackings following the ASTM D5045-14 standard specifications for the three-point bending test [35]. The stress intensity factor for bending specimens is defined as:

$$(K_I) = \frac{P_{max}}{BW^{1/2}} f\left(\frac{a_0}{W}\right), \tag{1}$$

with

$$\frac{a_0}{W} = p, \tag{2}$$

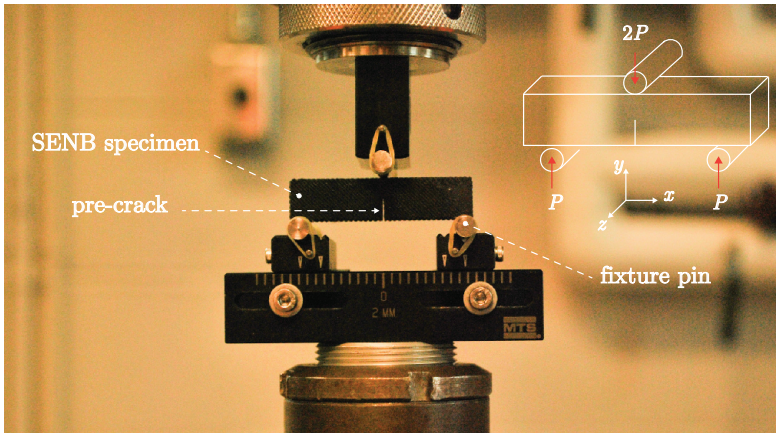

Figure 2: Three-point bending fixture for testing pre-cracked SENB specimens and measuring the fracture properties from the load-displacement curve recorded by the electromechanical machine. The fixture includes specific adapters for the flexural load transfer to the bottom cylinders in contact with the specimen, while the top adapter is stationary.

$$f(p) = 6p^{1/2}\frac{1.99 - p(1-p)(2.15 - 3.93p + 2.7p^2)}{(1+2p)(1-p)^{3/2}}, \tag{3}$$

where P_{max} and a_0 state the peak load recorded during testing and the pre-crack length measured after failure by optical microscopy, respectively. W and B are the specimen's width and thickness, as shown in Figure 1a, with $W = 2B$ and $0.45 < a_0/W < 0.55$. This is valid for specimens for which $S/W = 4$, with S being the gap between the testing fixture cylinders for the load transfer.

2.2.2. Mesoscale characterization by stereoscopic digital image correlation

Figure 3 shows the Correlated Solutions stereomicroscopic DIC framework, including the Olympus SDF PLAPO 1.6XPF microscope with two Grasshopper3 GS3-U3-50S5M high-resolution cameras for the images acquisition at a frame rate of 4 fps, controlled by the software Vic-Snap (Correlated Solutions). We loaded the miniature CT specimens in the MTS Insight electromechanical machine with a 50 kN load cell installed and at a crosshead speed of 0.5 mm/min to follow the crack propagation dynamics by DIC.

We adjusted the microscope magnification to the crack propagation speed of each stacking to follow the damage evolution during mechanical testing. The brittleness of the $\bar{x}\bar{y}$ specimens with $0^\circ - 90^\circ$ stacking entailed a magnification below 1, resulting in a region of interest measuring around 5.2×3.2 mm^2. For all the other configurations, we tuned the x, y, and z precision platform position and microscope magnification above 1 to track the crack propagation over a region of interest (ROI) of 4×2.5 mm^2 on the CT specimen surface during Mode I delamination. We analyzed the images with the subset-based software for correlation Vic-3D 7 (Correlated Solutions). A subset size spanning from 91 to 95 pixels,

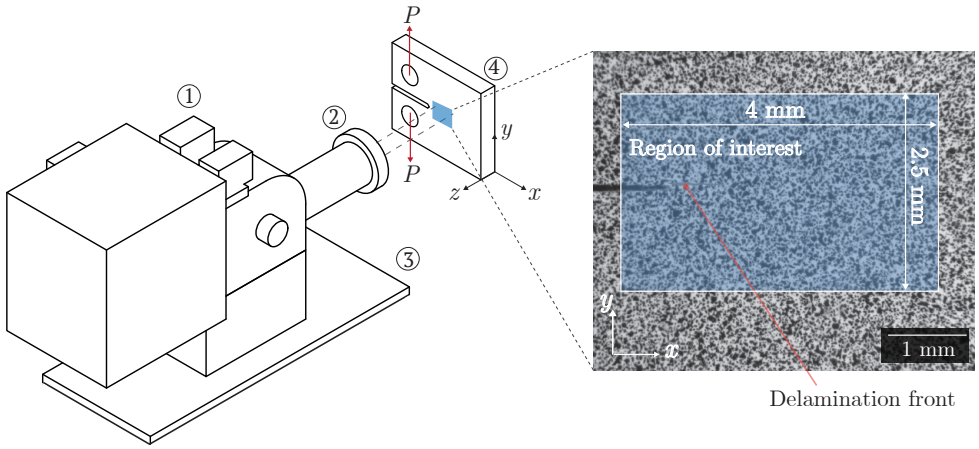

Figure 3: Images acquisition setup for microstereoscopic DIC and region of interest over the patterned miniature CT specimen surface. Two Grasshopper high-resolution cameras (1) installed on the stereomicroscope enabled the timed image acquisition. We ensured the microscope head (2) correct positioning using the precision movement stage (3) for the x, y, z microscope alignment with the region of interest over the specimen's surface (4). We defined the size of the region of interest over the specimens' surface to track the damage propagation at the delamination front, despite the specimen's rigid body motion.

a step of 6 to 7 pixels, and a strain filter of 13 to 15 delivered full displacement and strain fields over the ROI by solving the correlation problem based on zero normalized squared differences, as described in [37]. We extracted and plotted the vertical displacement (V), the vertical Lagrangian strain (ε_{yy}), aligned with the loading direction, and the confidence (θ) fields as an estimate of the damaged area. A positive θ states indeed the missed pixels match between a reference and deformed image due to excessive local strains, noise, or damage propagation [38, 39]. Therefore, we defined a threshold of 0.02 pixel to associate the θ increase to the damage nucleation and propagation, by direct comparison with the DIC images obtained for specimens with $0° - 90°$ stacking under interlayer delamination. Due to the reduced region of interest size, we could not derive crack-resistance curves for the different specimen configurations.

2.2.3. Fractography

After failure, we measured the SENB specimens' pre-crack length on the fracture surface with an Olympus SZX-12 optical microscope (12.5× magnification) to define the fracture properties. When needed, we cut the specimens using liquid nitrogen and coated the inspected surface with a 20 nm thick chromium layer to favor the interaction with the source electron beam. We inspected the specimens' fracture surface and cross-section with the Hitachi-TM3030Plus desktop SEM (15kV accelerating voltage) to identify the architectural features governing the damage advancement.

2.3. Microscale characterization by X-ray tomography

We studied the specimens' three-dimensional porosity dispersion and microscale fibers' distribution by X-ray tomography. After failure, we carved with a manual precision saw a representative cylindrical specimen having a height of 3 mm and a radius of 1.5 mm from the dogbone specimens' center region, whose mechanical properties are known. We then installed the specimen on the sample holder in the ZeissRadia™ 520 Versa X-ray computed tomography equipment. The source power, voltage, and magnification of 7 W, 80 kV, and 10×, respectively, allowed to discern individual fibers having a diameter of 7.5 μm at a pixel size of 0.75 μm, with eight individual high-resolution scans. Taking several scans and juxtaposing them in a $1 \times 1 \times 1.3$ mm^3 cuboid enables a total field of view (FoV) of approximately four layers for the characterization of the layer stacking and their interfaces in the same FoV. With the help of OpenFiberSeg, an open-source segmentation tool developed by Sosa-Rey et al. [40], we identified individual fibers, mesoscale porosity, and intrafilament porosity and tracked them in 3D.

3. Results and discussion

3.1. Mechanical characterization

3.1.1. Elastic properties

Figure 4 illustrates a typical stress (MPa)- strain (-) curve for each Type IV dogbone stacking, namely 0°, 90°, and $0° - 90°$. We recorded the highest ultimate stress for specimens loaded in the filaments' direction, whose mechanical response was driven by the high-strength

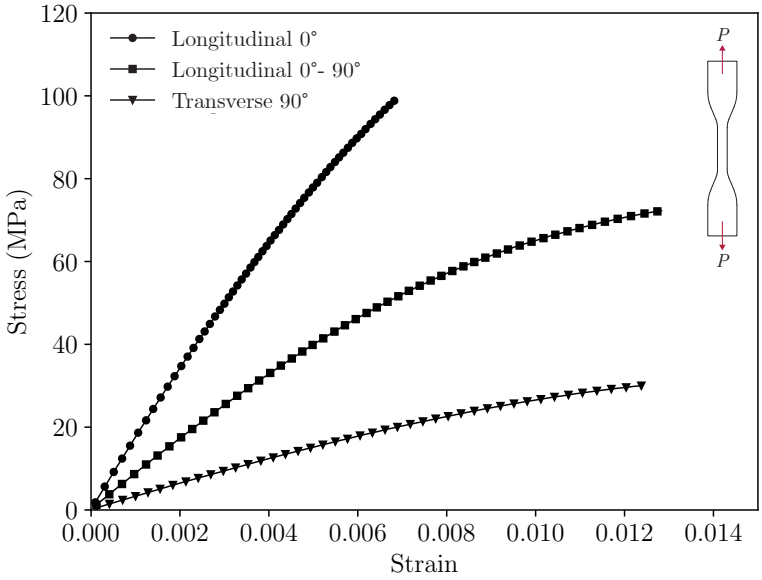

Figure 4: Typical stress (MPa)- strain (-) curves for Type IV dogbone specimens with 0° (longitudinal), 90° (transverse), and $0° - 90°$ stacking under tensile load. The ultimate stress and tensile modulus are maximized for specimens loaded along the reinforced filaments' direction. The addition of 90° oriented filaments deteriorates the strength and stiffness due to the filaments' interfaces' mechanical weakness under load and to the reinforcement misalignment with the loading direction.

Table 2: Average longitudinal and transverse in-plane elastic properties measured for Type I and Type IV CF PEEK specimens under tensile test. For each property, we report the 95% confidence intervals.

E_l (GPa)	E_t (GPa)	$E^{0°-90°}$ (GPa)	ν_{12}
16.6 [±0.8]	3.2 [±0.2]	9.7 [±0.5]	0.36 [±0.03]

reinforcement. The presence of reinforced filaments oriented perpendicularly to the loading direction decreased the specimens' strength, resulting in the ultimate stress drop by $\sim 1/3$ for specimens with $0° - 90°$ stacking and by 2/3 for specimens with 90° stacking, when compared to specimens with 0° stacking. Table 2 summarizes the average longitudinal and transverse elastic properties with the corresponding 95% confidence intervals. The measured average longitudinal modulus (E_l) of 16.6 GPa is comparable with that reported in the supplier data sheet for injection-molded specimens (17.5 GPa) [34], suggesting that the printing parameters selection was successful. The computed E_t is $\sim 20\%$ of the longitudinal tensile modulus mainly due to the fibers' orientation transversely to the loading direction. Moreover, during printing, the chamber temperature was significantly below the recommended value (*i.e.*, 250°C) [34], thus hindering the molecular diffusion at the filaments' interfaces and potentially resulting in relatively low transverse properties. The partial misalignment between the reinforcement and the loading direction for specimens with $0° - 90°$ oriented layers results in a 9.7 GPa stiffness, intermediate between the previously described scenarios. The computed Poisson's ratio (0.36) is slightly higher than the values reported in the

Table 3: Average longitudinal and transverse in-plane elastic properties predicted by dual scale FFT homogenization of real meso and microstructures for CF PEEK specimens under tensile test. For each property, we report the 95% confidence intervals [42].

E_l (GPa)	E_t (GPa)	$E^{0°-90°}$ (GPa)
15.6 [±1.5]	4.4 [±1.3]	8.8 [±1.2]

literature for 3D printed short fiber-reinforced composites [27, 41].

We compared the experimental results with the elastic properties prediction using the multiscale fast Fourier transform (FFT) homogenization approach developed ad-hoc for additively manufactured composites described in [42]. Table 3 summarizes the average E_l, E_t, and $E^{0°-90°}$ resulting from the dual-scale homogenization of real meso and microstructures inspected by X-ray tomography, with the corresponding 95% confidence intervals. The predictions agree with the experimental results, as they take into account the 3D process-induced porosity dispersion and fibers alignment observed for 30 w% carbon fiber-reinforced Ensinger Victrex PEEK. The slight overestimation of the transverse modulus could be attributed to the interface's incomplete adhesion, neglected in the homogenization approach.

3.1.2. Fracture properties

Figure 5 compares typical force-displacement curves and fracture toughness found for $\bar{z}$ and $\bar{x}\bar{y}$ SENB specimens with different stacking sequences under three-point bending. The load-displacement curves variability within each specimen set, defined as the four tested specimens with the same stacking and printing strategy, is discussed in Appendix A.1. We refer to the interlayer and intralayer failure for $\bar{z}$ and $\bar{x}\bar{y}$ specimens, respectively, according to the different crack propagation mechanisms. The intralayer failure involves the crack propagation along filaments' interfaces for specimens with 0° stacking and across filaments for specimens with 90° and $0° - 90°$ stackings. Overall, we recorded a weaker force-displacement response for specimens undergoing interlayer damage, when compared to their counterpart under Mode I intralayer failure, as shown in Figure 5a. The lowest peak loads correspond to specimens with 0° stacking for a crack propagating both between and within deposited layers.

We observe the greatest peak load enhancement for specimens with 90° stacking under intralayer failure, more than twice their 0° counterpart. This behavior conforms to the different crack propagation mechanisms leading to failure. The damage nucleates and propagates along weakly bonded interfaces for specimens under interlayer delamination and for specimens with 0° stacking under intralayer failure. The intralayer delamination of specimens with $0° - 90°$ and 90° stackings involves the tough composite filaments breakage instead. Analogously, the energy-intensive damage of reinforced filaments results in higher fracture toughness and thus stress intensity factors under the assumption of straight crack propagation, as shown in Figure 5b. The K_{IC} 95% confidence interval superposition for specimens under interlayer failure highlights their statistical equivalence due to the incomplete layers' bonding during deposition. The K_{IC} of specimens with 0° stacking under intralayer failure

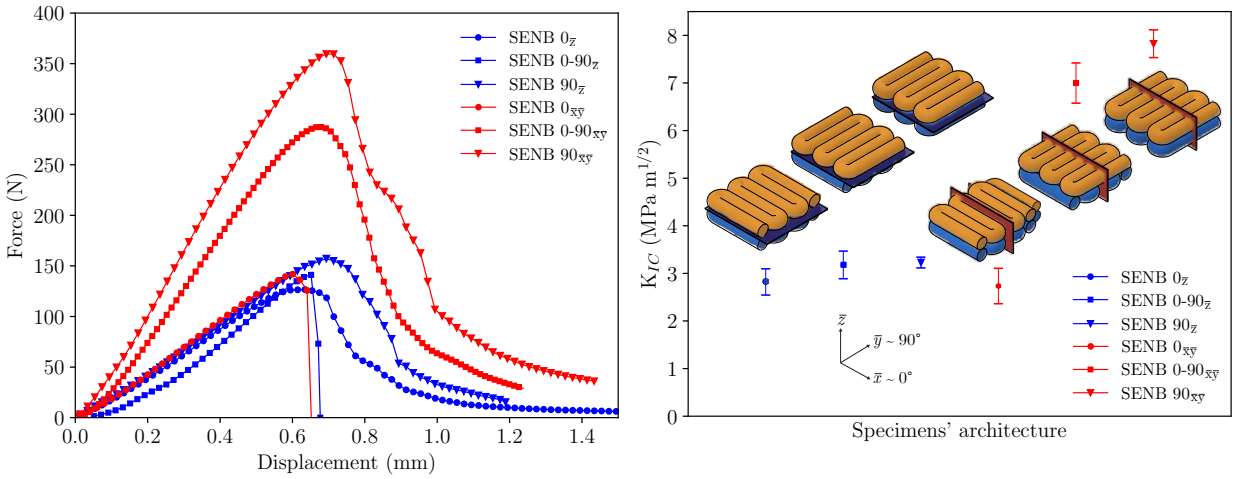

(a) (b)

Figure 5: Typical load-displacement response and average stress intensity factors measured for SENB specimens with different stackings under three-point bending. (a) For each stacking, the recorded peak load is lower for specimens undergoing interlayer failure (in blue), when compared to the intralayer failure (in red). The greatest peak load increase is recorded for specimens with $0° - 90°$ and $90°$ stackings under intralayer failure due to the crack propagation across composite filaments. (b) The K_{IC} 95% confidence intervals highlight the significant fracture toughness gain when the delamination involves the filaments breakage (red planes), instead of propagating along layers' and filaments' interfaces (blue planes).

falls in the same range found for specimens under interlayer delamination. The equivalent stress intensity factor emphasizes the comparable weak filaments' entanglement between and within FFF layers due to their analogous thermal history and the printing speed in the manufacturing phase [43]. Moreover, this observation suggests that there is no statistically different adhesion strength, whether the crack propagates between FFF layers or between filaments within the same layer. The K_{IC} increases when the failure involves the filaments' breakage. It has to be mentioned that the low specimens' number affects the results' dispersion and the confidence intervals' superposition. In Figure 5b, we observe an average stress intensity factor increase from 2.7 MPa m$^{1/2}$ to 7.8 MPa m$^{1/2}$ from the 0° to the 90° stacking for specimens under intralayer failure due to the crack propagation across composite filaments, tougher than the interface. The $0° - 90°$ stacking delivers an intermediate K_{IC} between the 0° and 90° configurations due to the coexistence of perpendicularly oriented plies.

3.2. Full-field strain measurements during delamination

The analysis of the confidence (θ), full displacement (V), and lagrangian strain (ε_{yy}) contours highlighted the primary damage nucleation and propagation mechanisms for CT specimens with $0° - 90°$ and $\pm 45°$ stackings under Mode I interlayer and intralayer delamination.

We report the corresponding force (N)- displacement curves recorded by the electromechanical machine in Appendix B. Figure 6 shows the confidence (θ) and ε_{yy} distribution

evolution at the crack tip for specimens with $0° - 90°$ stacking under **interlayer** delamination, before and after the peak load.

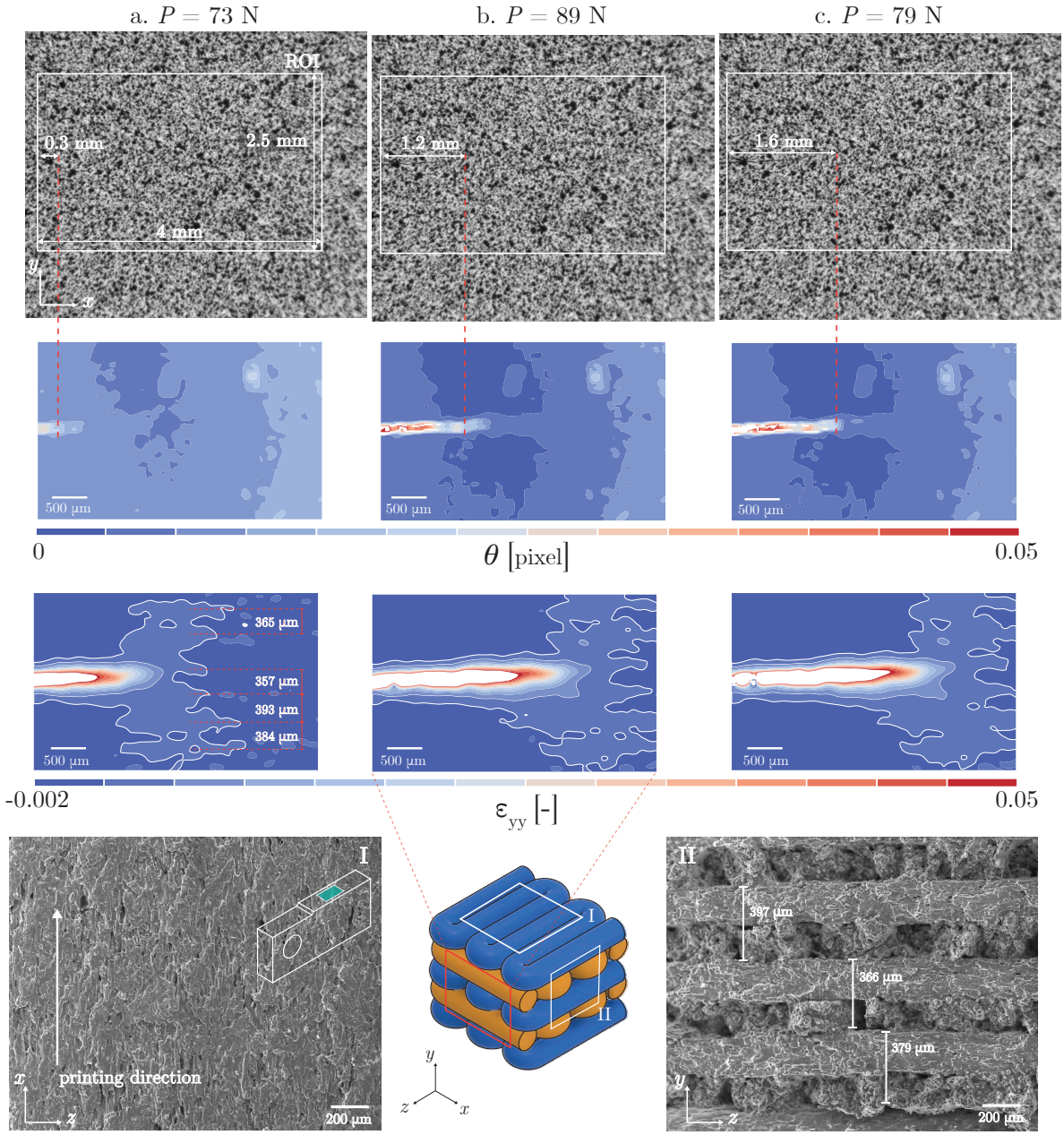

Figure 6: Full strain measurements and confidence distribution for CT specimens with $0° - 90°$ stacking undergoing interlayer failure before and after the peak load (89 N), and SEM inspection of (I) the fracture surface and (II) cross-section. The confidence distribution reveals a crack growth from 0.3 to 1.6 mm within the ROI. The ε_{yy} contour exhibits periodic heterogeneities along the y axis, corresponding to the weak $0° - 90°$ layers' interfaces, as revealed by the bi-layer gap estimated by SEM over the cross-section (II). The SEM inspection of the smooth fracture surface (I) highlights the absence of fibers and the crack propagation over a single interface due to the incomplete layer bonding during printing.

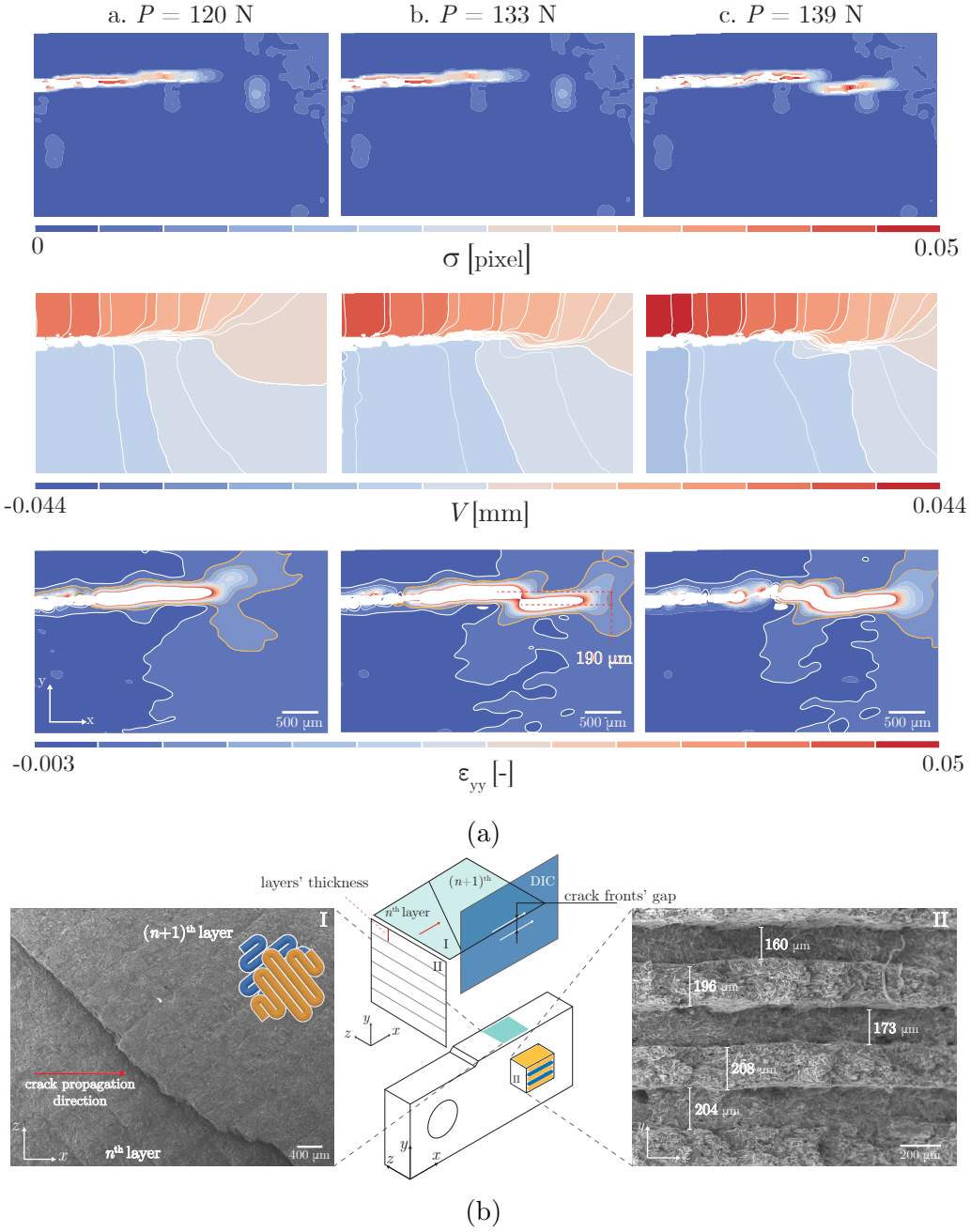

Figure 7: Full-field measurements and SEM inspection for CT specimens with ± 45° stacking under interlayer failure. (a) The θ contour reveals the presence of two damage propagation fronts, as highlighted by the V symmetric contour step alteration and by the multiple lobes distribution (in yellow) in the ε_{yy} contour. We measured the gap between the two delamination fronts (190 μm) in the ε_{yy} contour. (b) The fracture surface inspection (I) revealed the crack transfer from the pre-cracked interface to the adjacent one, exposing two layers with 45° and −45° oriented filaments. We measured the 188 μm average layers' thickness over the specimen's cross-section by SEM inspection (II), in agreement with the crack fronts gap estimated from the DIC strain contours, supporting the crack bifurcation hypothesis.

We interpret the positive (> 0.02) θ distribution as an estimate of the crack length growth within the region of interest from 0.3 to 1.6 mm under mechanical testing, resulting in the pixels match loss during correlation. The ε_{yy} field follows the lobes distribution expected for Mode I failure, with the stress concentration (in red) along the delamination front. The white region around the advancing crack corresponds to the measurements discontinuity and the local strain peak, out of scale. The periodic ε_{yy} heterogeneities distribution along the y axis in Figure 6 follows the $0^\circ - 90^\circ$ filaments' interfaces arrangement measured in 2D by SEM in the cross-section image view (II), with a gap of ~ 375 μm, equivalent to the cumulative thickness of two layers. We can thus attribute the local strain concentration to the weakly bonded interfaces between 0° and 90° oriented planes, likely to fail under a Mode I load below 150 N, possibly due to the deposition process and layer stacking. The fracture surface inspection by SEM (I) suggests the absence of fibers at the layers' interfaces as a consequence of the filaments manufacturing process and shearing during extrusion. This results in a smooth crack propagation at the interface, and a constrained process zone, where the local strains are positive.

Figure 7a shows the vertical displacement, strain distribution, and confidence contour for specimens with $\pm 45^\circ$ stacking under interlayer delamination, right before the peak load $P = 139$ N.

The θ distribution exhibits two crack fronts, where the pixels matching is lost due to the damage nucleation and propagation. The V contour plot symmetry is altered by the damage bifurcation from the pre-cracked interface to a parallel adjacent layers' interface. Analogously, the ε_{yy} contour displays the presence of two strain concentration regions characterized by the lobes distribution at the crack tip due to the failure of adjacent interfaces, 190 μm apart from each other. The described DIC field heterogeneity was observed for three of the four tested specimens. We inspected the specimen's fracture surface (I) and cross-section (II) by SEM to correlate the contours heterogeneities with geometrical features. The fracture surface inspection by SEM in Figure 7b reveals the crack transition from the notched interface to the adjacent one, exposing two layers with filaments oriented perpendicularly, along the 45° and -45° directions. We measured an average layers' thickness of ~ 188 μm in the cross-section SEM image, approximating the distance between adjacent interfaces on the xy plane, as shown in Figure 7b. This interface's gap was consistent with the crack propagation fronts distance by DIC, suggesting the crack transition to the nearest weak interface due to the incomplete layers' adhesion. We did not observe this damage mechanism for specimens with $0^\circ - 90^\circ$ stacking, for which the failure propagates smoothly on the pre-cracked plane, as highlighted in Figure 6.

The **intralayer** delamination of CT specimens involved higher loads and displacements, when compared to the interlayer counterpart. The significant rigid body motion experienced under loading by specimens with $0^\circ - 90^\circ$ stacking required a lower microscope magnification to successfully track the crack advancement over a 5.2×3.2 mm^2 surface.

Figure 8 highlights that the presence of filaments oriented along the y direction stretches and alters the V field symmetry for specimens with $0^\circ - 90^\circ$ stacking under **intralayer** failure. We observed a rapid crack growth from 0.3 mm to 2.6 mm in the θ contour, after the peak load (~ 1676 N). The ε_{yy} contour follows the lobes distribution at the crack tip,

and it presents strain concentration areas along the crack front due to the breakage of 90° oriented filaments after the peak load (highlighted in yellow). The contours are noisier, when compared to specimens with the same stacking under interlayer failure due to the complex damage propagation mechanism involving the breakage of the bulk composite material as

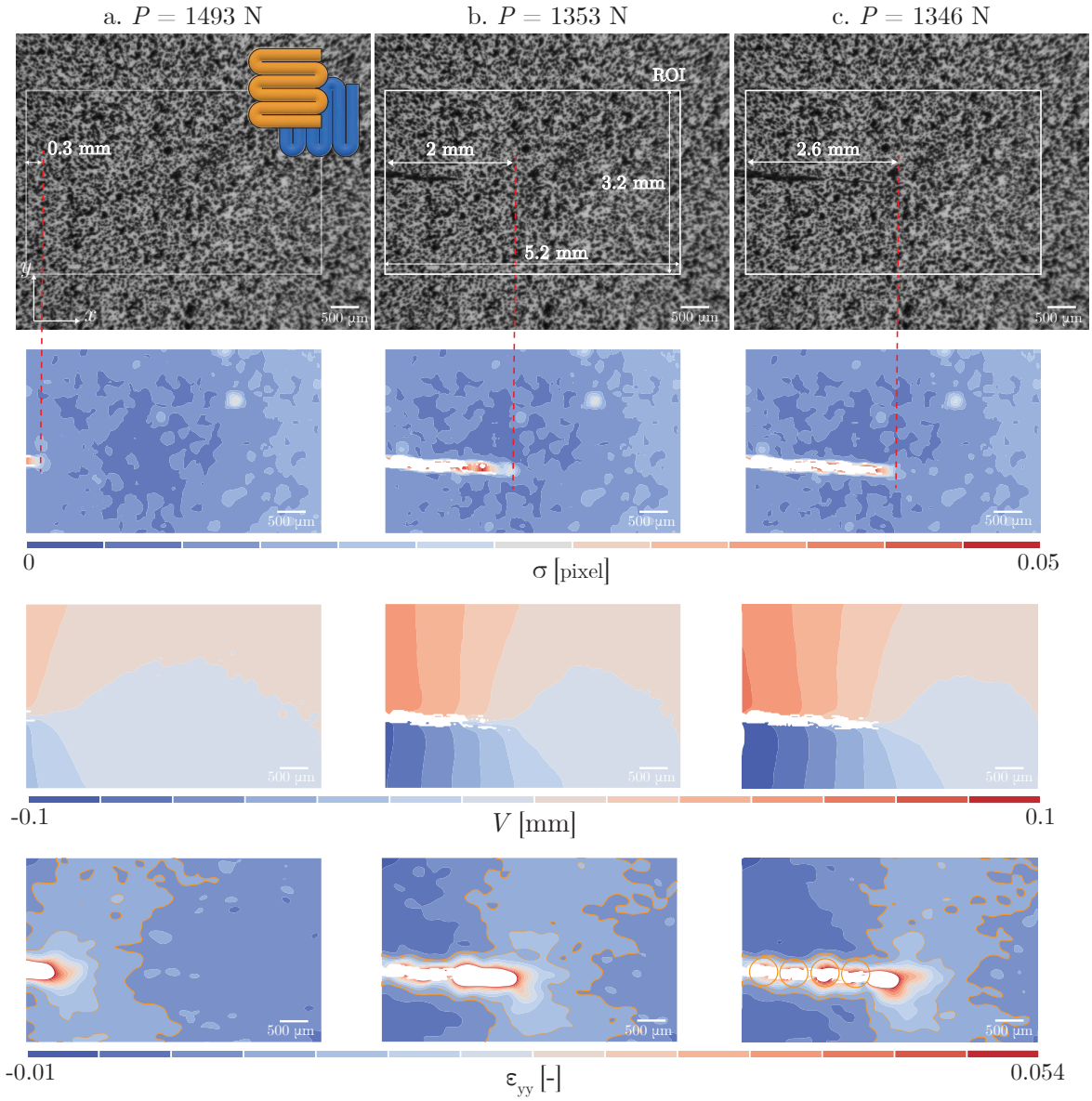

Figure 8: Raw DIC images and contour plots for specimens with $0° - 90°$ stacking under intralayer delamination. The crack rapidly grows from 0.3 mm to 2.6 mm after the peak load (1676 N), as observed in the confidence (θ) contour. The presence of filaments aligned perpendicularly to the loading direction (90°) hinders the crack propagation, stretching the V contour along the y axis. The ε_{yy} distribution is affected by strain concentration areas due to the 90° oriented filaments progressive breakage and exhibits a wider lobes strain concentration zone (in yellow circles), when compared to the ε_{yy} contour for interlayer specimens with the same stacking analyzed in Figure 6.

well as of weak filaments' interfaces.

Figure 9a shows the displacement and strain contour plots for specimens with ±45° stacking under intralayer failure. The V field symmetry is altered by the filaments' orientation, resulting in a field stretching along the ±45° directions. Analogously, local ε_{yy} strain con-

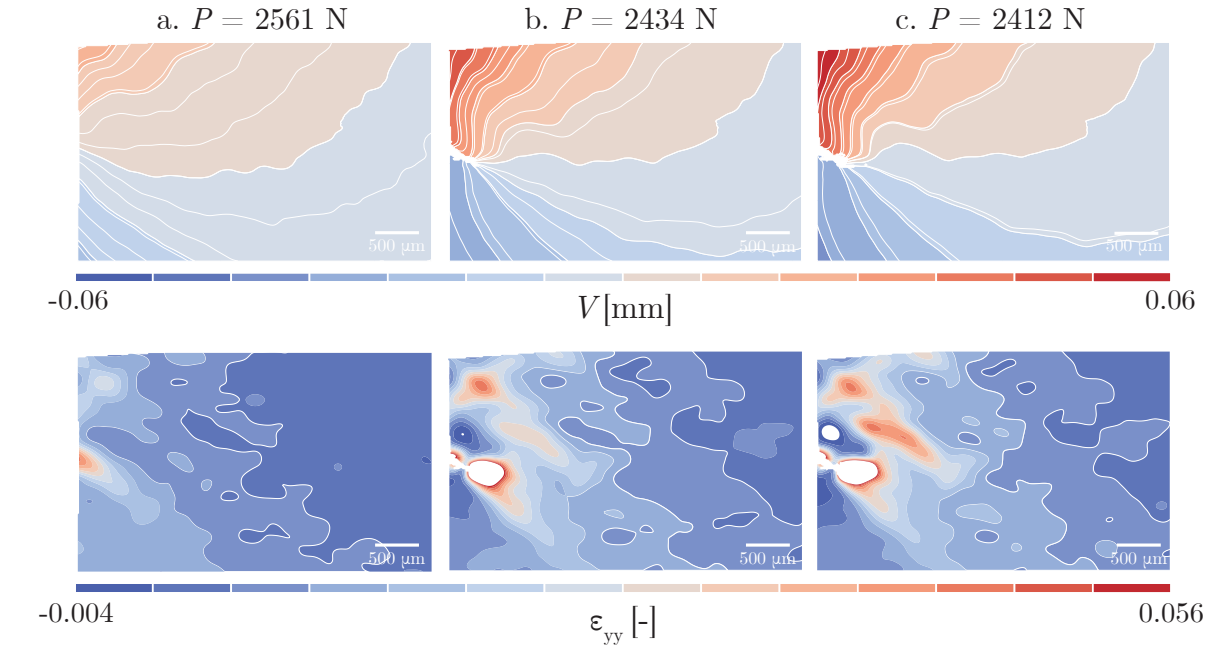

(a)

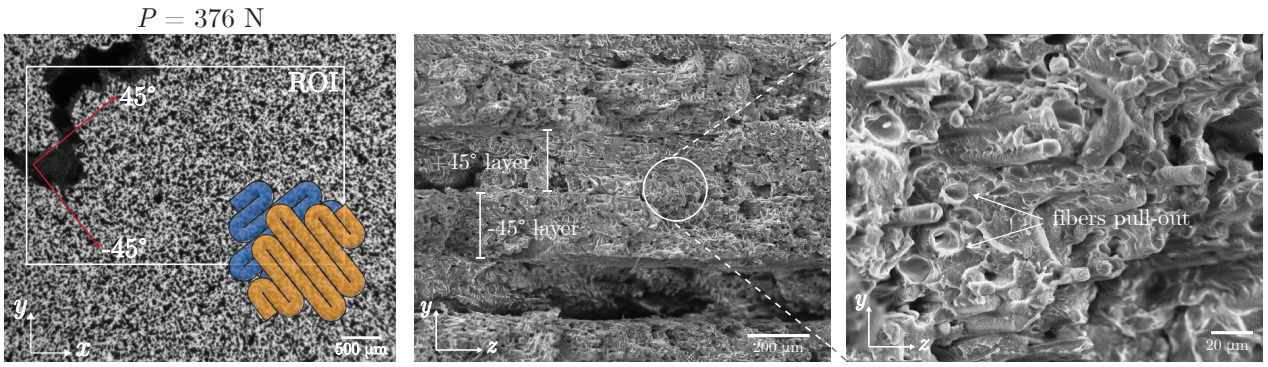

(b) (c)

Figure 9: Full displacement and strain measurements for CT specimens with ±45° stacking undergoing intralayer failure, raw DIC image right after the crack bifurcation, and SEM inspection of the specimens' cross-section. (a) The V shape ε_{yy} distribution highlights the crack propagation along weekly bonded ±45° oriented filaments' interfaces. The crack bifurcation observed in the ε_{yy} contour results in the *zig-zag* damage propagation path shown in the DIC image right after failure (b), for a load drop to P=376 N. The rigid body motion along y and z caused the correlation loss at the top left corner of the region of interest. (c) The cross-section SEM inspection reveals the fibers' alignment with the deposition direction at the filaments' core and the poor interface bonding.

centration areas follow the ±45° poorly bonded filaments' interfaces, resulting in the *zig-zag* crack propagation between and through perpendicularly oriented composite filaments. After reaching the peak load of 2646 N, the load decreased progressively while damage nucleated along the ±45° interfaces, prior to its drop to $P = 376$ N due to quasi-brittle failure conforming to the *zig-zag* crack path highlighted in the DIC image in Figure 9b. The SEM inspection of the specimen's cross-section in Figure 9c suggests the contrast between the highly charged filaments core and the weakly entangled layers' interfaces, promoting delamination under loading. Moreover, we identify the porosity originating from the fibers' pull out during the specimen cutting for the inspection.

For the totality of the tested specimens, we obtained continuous displacement and strain fields around the propagating discontinuity, independently from the local phenomena driving the failure of specimens with different stackings. The average displacement and strain resolution, dependent on the subset, step, and magnification, was globally ~ 350 μm and ~ 330 μm, respectively, enabling the validation of mesoscale damage models through the comparison of the finite element simulation results with the nodal V and ε_{yy} values by DIC.

3.3. X-ray tomography

The post-mortem X-ray specimens inspection delivered insight into the qualitative three-dimensional fibers and porosity dispersions resulting from the filament deposition pattern, with a focus on the layers' interface. We inspected exclusively one specimen, cut from a Type I dogbone with $0° - 90°$ stacking, due to the long time required for the X-ray scanning and images segmentation ($\sim$ 20 days). Nevertheless, the observed qualitative fibers and pores distribution could be representative of the FFF process-related dispersion for specimens with alternate stackings.

In Figure 10, we show the contours resulting from the fibers' length and porosity slices sum through the representative cube along the z and x directions, projected on the xy (I) and yz (II) planes, respectively. We associated arbitrary values to the scale bar upper and lower bounds for a qualitative analysis of the fibers' and pores' distribution. In the fiber and pores density plots I, we can identify the 0° and 90° oriented layer stacking, with fibers aligned along the x and out of plane directions, and bounded by interlayer porosity. The fibers density II view highlights the fibers distribution at the filaments' core, as opposed to the pores concentration at the layers' interfaces, whose pattern is recognizable in dark blue. One of the possible causes of the fibers' concentration at the filaments' core can be the nozzle shearing during the extrusion, delivering layers' interfaces mechanically weaker than the bulk composite. Both the I and II porosity density contours point out that the multiscale porosity concentrates at the layers' interface, following the waves induced by the presence of 90° oriented filaments (II). This high interlayer porosity promoted the damage nucleation at the layers' interfaces and the crack advancement over parallel interfaces under opening mode load. The interface's low fibers concentration and high porosity density, highlighted by X-ray tomography, further clarified the phenomena observed by DIC during interlayer failure, such as the absence of fibers on the fracture surface of specimens with $0° - 90°$ stacking and the damaging of parallel ±45° oriented interfaces under loading.

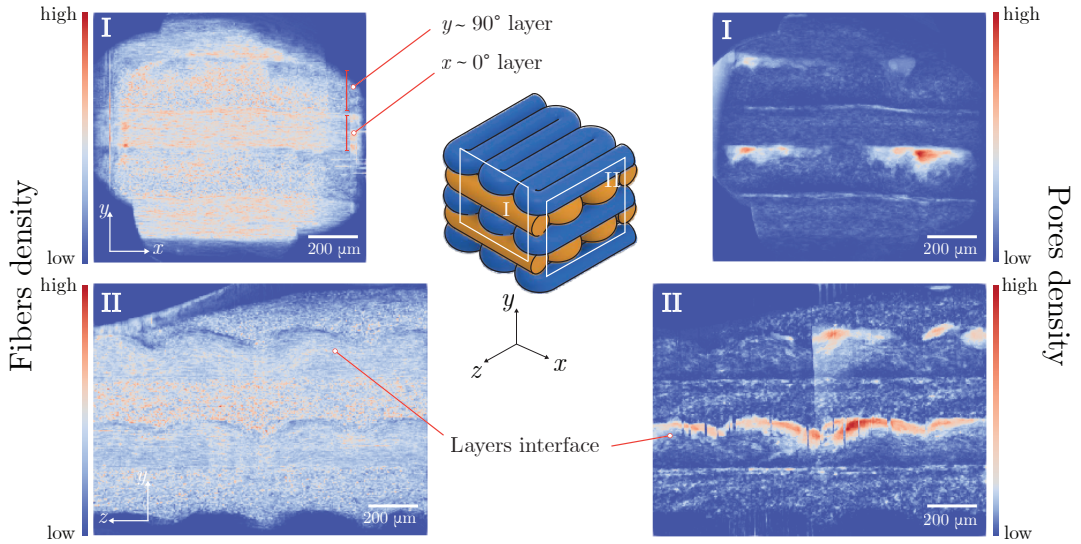

Figure 10: Qualitative fibers and porosity distribution by X-ray tomography across a representative volume of 3D printed CF-reinforced PEEK with $0° - 90°$ stacking. The fibers density view I highlights the fibers' alignment with the deposition direction along 0° and 90° oriented layers and their concentration at the filaments' core. (II) The highest pores density is observed at the layers' interface on both projection planes (I, II), promoting the damage and failure of parallel interfaces under Mode I loading.

4. Conclusions

We investigated the elastic and fracture behavior of 3D printed fiber-reinforced PEEK to guide the design of reliable, high-performance components and to promote the development of representative modeling approaches. We emphasized the influence of the multiscale architectural features (e.g., porosity, weakly entangled interfaces) on the failure of composites manufactured by FFF through macroscopic standard tests (elastic and fracture), and local meso and micro-scale characterization by microstereoscopic DIC, SEM, and X-ray tomography. The macroscopic characterization highlighted the 3D printed composites' anisotropy under tensile testing. We recorded a tensile modulus drop below 20% of its longitudinal value for specimens with filaments' interfaces oriented perpendicularly to the load direction. The poor filaments' adhesion during manufacturing and the lack of fibers in the loading direction could be two of the possible causes of this stiffness deterioration. Analogously, the three-point bending tests suggested that the filaments orientation perpendicularly to the crack propagation direction increases the specimens' fracture toughness. Moreover, the crack propagation at the layers and filaments' interfaces results in equivalent fracture energy due to the similar thermal history during deposition and thus interface adhesion. However, higher fracture energy is required when the failure involves the composite filaments breakage. The stress intensity factor measured for specimens with $0° - 90°$ stacking under interlayer delamination is indeed around half of that estimated for specimens with the same stacking under intralayer failure.

The DIC's strain and displacement fields unveiled the local phenomena driving the interface damage of CT specimens with $0° - 90°$ and $\pm 45°$ stacking. The crack propagates

smoothly along the weakly bonded $0° - 90°$ layers' interfaces, as opposed to the crack transition to the adjacent interface observed by DIC and SEM for specimens with $\pm 45°$ stacking. The crack propagation between filaments involves higher local strains and conforms to the orientation of the interfaces, following a *zig-zag* path for specimens with $\pm 45°$ stacking. The high displacement and strain measurements spatial resolution promotes the development and validation of mesoscale damage models for FFF composite interfaces by directly matching the measured and predicted nodal values extracted for each subset edge. The observation drawn from the V and ε_{yy} contours were supported by the specimens' architecture inspection by SEM and X-ray tomography. The SEM images analysis and the X-ray images segmentation highlighted the fibers' concentration at the filaments core and the pores concentration at the layers' interfaces, further explaining the premature interface failure under loading. The presented outcomes guide the design of reliable, high-performance FFF composite structures and deliver guidelines for process optimization, suggesting the reinforcement filaments deposition along the most solicited directions and the careful layer stacking selection ($0° - 90°$ or $\pm 45°$) based on the crack propagation and loading directions to avoid premature interface failure. Moreover, the described characterization approach can be extended to studying the failure of various anisotropic materials (*e.g.*, natural fiber composites, composites by injection molding, 3D printed continuous fiber-reinforced composites), whose meso/micro structural features affect the crack nucleation and propagation under operating conditions.

Acknowledgements

We acknowledge the technical support of Mr. Dogan Arslan for the SEM images acquisition and of Charles Desjardins for the pendulum pre-cracking system design. We acknowledge the financial and technical support of the Safran Industrial Research Chair on Additive Manufacturing of Organic Matrix Composites (AMOMC) and the financial support of the Natural Sciences and Engineering Research Council of Canada (NSERC, CRDPJ 514761-1).

Appendix A. SENB specimens load-displacement curves and SEM inspection

Appendix A.1. SENB specimens load-displacement curves

In Figure A.11, we report the load-displacement curves for all the tested SENB specimens manufactured with different stacking and printing strategies. Overall, the curves are reproducible in terms of peak load and fracture behavior for a given layer stacking and crack propagation type (interlayer or intralayer). However, we observe a few discrepancies for $\bar{x}\bar{y}$ specimens with $0°$ stacking (Figure A.11b), whose peak load varies between ~ 100 and ~ 150 N, possibly due to the weak filament interface adhesion and its sensitivity to the presence of manufacturing defects. Moreover, both stable and unstable crack growth is observed for $\bar{z}$ specimens with $0° - 90°$ stacking under interlayer failure, as shown in Figure A.11c. The load-displacement curves variability in Figure A.11c for specimens with $0° - 90°$ stacking under interlayer propagation can be possibly attributed to the complex crack propagation mechanisms through alternate stackings. The fracture behavior discrepancies can be potentially attributed to the manufacturing defects, the feedstock material, and the specimens' pre-cracking, driving the damage nucleation, as discussed in [37].

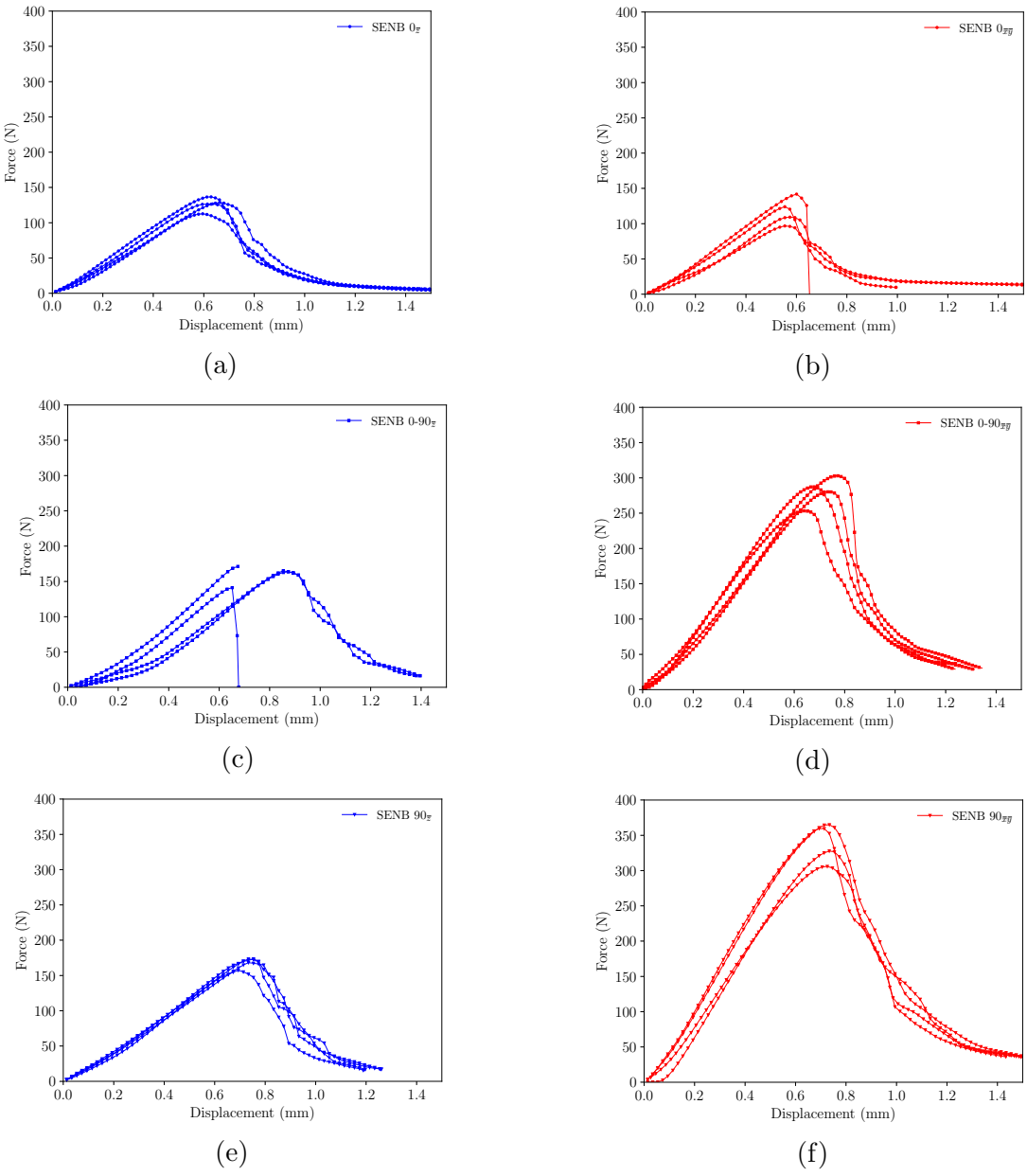

Figure A.11: Load-displacement response for $\bar{x}\bar{y}$ and $\bar{z}$ SENB specimens with 0° ((a), (b)), $0° - 90°$ ((c), (d)), and 90° ((e), (f)) stackings under three point bending test. Overall, the response and the fracture behaviors are relatively consistent in terms of peak load and crack propagation for all the configurations. However, $\bar{x}\bar{y}$ specimens with 0° stacking ((b)) and $\bar{z}$ specimens with $0° - 90°$ stacking show both sudden failure and dynamic crack growth possibly due to the reduced filament contact surface and poor filament interface adhesion, respectively.

Appendix A.2. SENB specimens' cross-section and fracture surface inspection by SEM

After failure, we inspected the SENB specimens cross-section and fracture surface to investigate the layer and filament contact area influence on the fracture toughness.

Overall, the SEM images in Figure A.12 highlight the reduced volumic interfilament porosity content and the smooth fracture surfaces of specimens with 0°, 0° − 90°, and 90° stackings under interlayer failure. However, the cross-section inspection for $\bar{x}\bar{y}$ specimens with 0° stacking revealed the presence of diamond-shaped pores between filaments. These discontinuities are more severe than for alternate stacking (0° − 90°), possibly due to the deposition strategy during manufacturing. The reduced filament contact surface hindering the interfaces' molecular diffusion could partially explain the equivalent fracture toughness involved in the interlayer failure of specimens with 0°, 90°, and 0°−90° stacking and intralayer

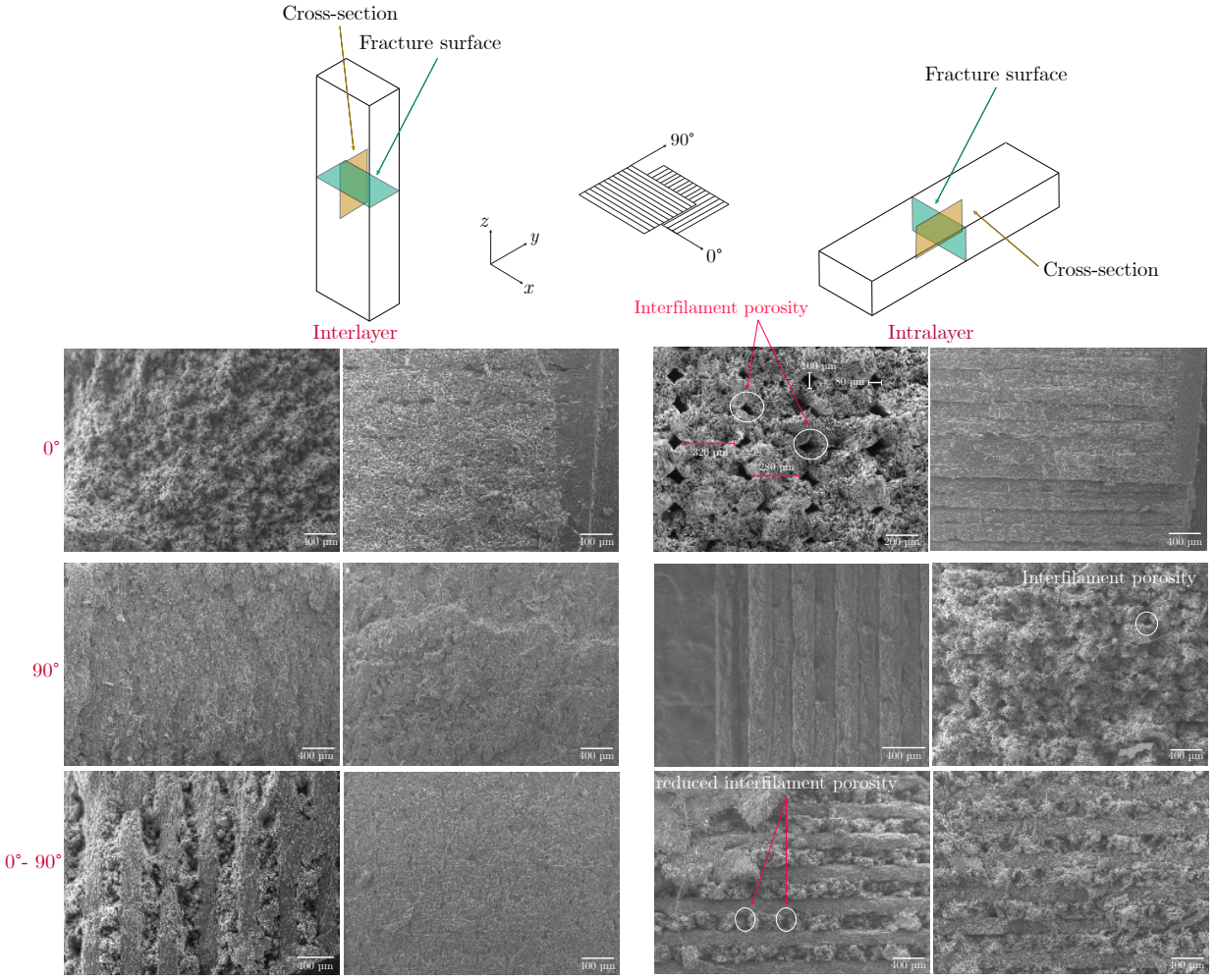

Figure A.12: Fracture surface and cross-section inspection by SEM for SENB specimens with 0°, 0°−90°, and 90° stacking after interlayer and intralayer failure. The printing parameters optimization delivers a fracture surface and cross-section where the interfilament porosity is hardly detectable, justifying the approximation of the real fracture surface with the theoretical one for the fracture toughness measurements. However, the interfilament porosity and lower filaments contact area observed over the cross-section of $\bar{x}\bar{y}$ specimens with 0° stacking explain the fracture toughness equivalence to that recorded for specimens under interlayer failure.

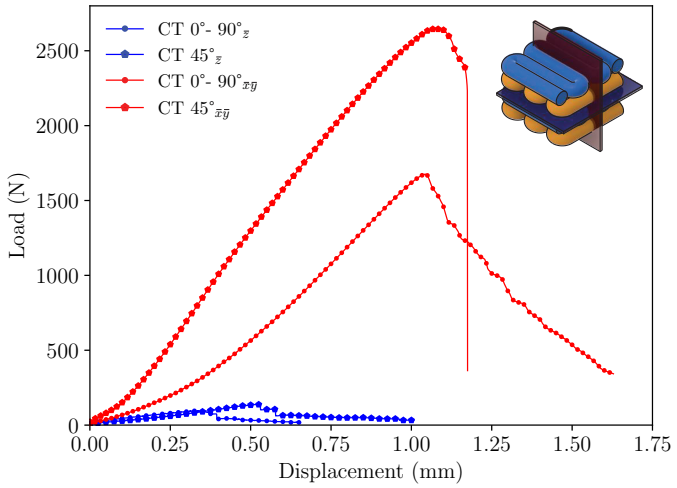

Figure B.13: Load (N)- displacement (mm) curves recorded using the Insight machine for CT specimens with $0^\circ - 90^\circ$, and $\pm 45^\circ$ stacking under interlayer (in blue) and intralayer (in red) delamination during the images acquisition for DIC. The curve recorded for specimens with $\pm 45^\circ$ stacking under interlayer delamination exhibits a step behavior possibly due to the progressive damage of multiple interfaces. The intralayer failure involves higher peak loads, when compared to the interlayer delamination due to the crack propagation across reinforced filaments.

failure of specimens with 0° stacking.

Appendix B. Compact tension test curves

Figure B.13 shows the Load (N)- Displacement (mm) curves recorded by the Insight machine during mechanical testing for the miniature CT specimens with $0^\circ - 90^\circ$ and $\pm 45^\circ$ stacking under interlayer and intralayer delamination whose failure was investigated by DIC. The peak loads observed for interlayer failure were more than ten times lower than those recorded during intralayer delamination for both $0^\circ - 90^\circ$ and $\pm 45^\circ$ stackings. The intralayer failure involved indeed the energy-intensive composite filaments breakage, as observed in the ε_{yy} contours by DIC and in the SEM inspections. Analogously, we can correlate the step load-displacement curve recorded for specimens with $\pm 45^\circ$ stacking under interlayer failure to the crack transfer from the pre-cracked interface to the adjacent one observed in the full-field measurements by DIC and in the fracture surface inspection by SEM. The peak load is maximized ($\sim$ 2650 N) for specimens with $\pm 45^\circ$ stacking under intralayer failure due to the crack propagation along filaments' interfaces as well as across filaments delivering the *zig-zag* crack path highlighted in the DIC contours in Figure 9.

Appendix C. Pendulum system design for the consistent specimens' pre-cracking

We designed a pendulum system for the SENB and CT specimens pre-cracking for fracture testing. Figure C.14 shows the supporting platform (1) holding the system steady during the impact force transferring from the hammer to the specimen's midplane. The

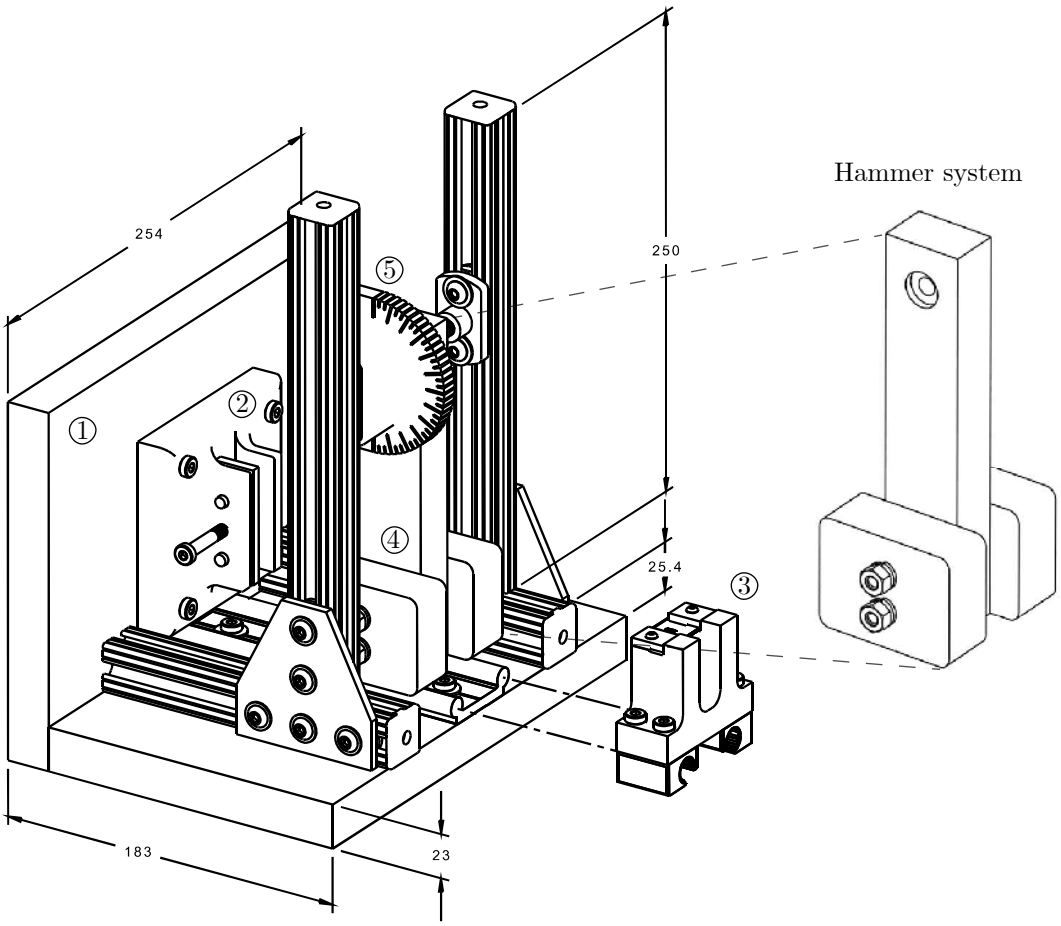

Figure C.14: Pre-cracking pendulum assembly for the fracture specimens' controlled notching. The framework includes a wooden platform (1) for stable positioning, a specimen (2) and a blade (3) holder for the precise pre-cracking, a hammer system (4) with a graduated scale (5) to select the impact force, and a magnifying glass for the careful alignment with the specimens midplane. The dimensions are in millimeters.

specimen is positioned in the holder (2), adjustable to the different configurations through a screws system. The blade is aligned with the specimen's midplane through a blade support (3) installed on low friction rails and including a magnifying glass to ease the blade positioning at the interface to pre-crack. The hammer system (4) includes a wooden handle and a steel head for the force transfer to the blade, tightened to the handle through threaded rods. Through a preliminary study, we identified the impact forces required to pre-crack $\bar{x}\bar{y}$ SENB and CT specimens and correlated them with the hammer fall angle in the graduated system to ensure consistency and repeatability. The study revealed that the pendulum impact force was too high to pre-crack $\bar{z}$ specimens, whose poor layers' adhesion resulted in excessive damage before testing. Compared to conventional solutions, the presented system's main advantages are the possibility to control the impact force, function of the hammer falling angle and the blade positioning to consistently pre-crack fracture specimens.

Bibliography

[1] H. L. Tekinalp, V. Kunc, G. M. Velez-Garcia, C. E. Duty, L. J. Love, A. K. Naskar, C. A. Blue, S. Ozcan, Highly oriented carbon fiberpolymer composites via additive manufacturing, Composites Science and Technology 105 (2014) 144–150. doi:10.1016/j.compscitech.2014.10.009.
URL https://linkinghub.elsevier.com/retrieve/pii/S0266353814003716

[2] T. D. Ngo, A. Kashani, G. Imbalzano, K. T. Nguyen, D. Hui, Additive manufacturing (3D printing): A review of materials, methods, applications and challenges, Composites Part B: Engineering 143 (2018) 172–196. doi:10.1016/j.compositesb.2018.02.012.
URL https://linkinghub.elsevier.com/retrieve/pii/S1359836817342944

[3] N. van de Werken, H. Tekinalp, P. Khanbolouki, S. Ozcan, A. Williams, M. Tehrani, Additively manufactured carbon fiber-reinforced composites: State of the art and perspective, Additive Manufacturing 31 (2020) 100962. doi:10.1016/j.addma.2019.100962.
URL https://linkinghub.elsevier.com/retrieve/pii/S2214860419311698

[4] L. Blok, M. Longana, H. Yu, B. Woods, An investigation into 3D printing of fibre reinforced thermoplastic composites, Additive Manufacturing 22 (2018) 176–186. doi:10.1016/j.addma.2018.04.039.
URL https://linkinghub.elsevier.com/retrieve/pii/S2214860417305687

[5] F. Touchard, L. Chocinski-Arnault, T. Fournier, C. Magro, A. Lafitte, A. Caradec, Interfacial adhesion quality in 3D printed continuous CF/PA6 composites at filament/matrix and interlaminar scales, Composites Part B: Engineering 218 (2021) 108891. doi:10.1016/j.compositesb.2021.108891.
URL https://linkinghub.elsevier.com/retrieve/pii/S1359836821002821

[6] P. Parandoush, D. Lin, A review on additive manufacturing of polymer-fiber composites, Composite Structures 182 (2017) 36–53. doi:10.1016/j.compstruct.2017.08.088.
URL https://linkinghub.elsevier.com/retrieve/pii/S0263822316329063

[7] X. Wang, M. Jiang, Z. Zhou, J. Gou, D. Hui, 3D printing of polymer matrix composites: A review and prospective, Composites Part B: Engineering 110 (2017) 442–458. doi:10.1016/j.compositesb.2016.11.034.
URL https://linkinghub.elsevier.com/retrieve/pii/S1359836816321230

[8] M. Luo, X. Tian, J. Shang, W. Zhu, D. Li, Y. Qin, Impregnation and interlayer bonding behaviours of 3D-printed continuous carbon-fiber-reinforced poly-ether-ether-ketone composites, Composites Part A: Applied Science and Manufacturing 121 (2019) 130–138. doi:10.1016/j.compositesa.2019.03.020.
URL https://linkinghub.elsevier.com/retrieve/pii/S1359835X19300995

[9] S. M. F. Kabir, K. Mathur, A.-F. M. Seyam, A critical review on 3D printed continuous fiber-reinforced composites: History, mechanism, materials and properties, Composite Structures 232 (2020) 111476. doi:10.1016/j.compstruct.2019.111476.
URL https://linkinghub.elsevier.com/retrieve/pii/S0263822319322706

[10] A. Stepashkin, D. Chukov, F. Senatov, A. Salimon, A. Korsunsky, S. Kaloshkin, 3D-printed PEEK-carbon fiber (CF) composites: Structure and thermal properties, Composites Science and Technology 164 (2018) 319–326. doi:10.1016/j.compscitech.2018.05.032.
URL https://linkinghub.elsevier.com/retrieve/pii/S0266353818300873

[11] D. Young, N. Wetmore, M. Czabaj, Interlayer fracture toughness of additively manufactured unreinforced and carbon-fiber-reinforced acrylonitrile butadiene styrene, Additive Manufacturing 22 (2018) 508–515. doi:10.1016/j.addma.2018.02.023.
URL https://linkinghub.elsevier.com/retrieve/pii/S2214860418303919

[12] C. Bellehumeur, L. Li, Q. Sun, P. Gu, Modeling of Bond Formation Between Polymer Filaments in the Fused Deposition Modeling Process, Journal of Manufacturing Processes 6 (2) (2004) 170–178. doi:10.1016/S1526-6125(04)70071-7.
URL https://linkinghub.elsevier.com/retrieve/pii/S1526612504700717

[13] K. Rodze, E. Harkin-Jones, M. Wegrzyn, P. Sharma, A. Zhigunov, Improvement of the layer-layer adhesion in FFF 3D printed PEEK/carbon fibre composites, Composites Part A: Applied Science and Manufacturing 149 (2021) 106532. doi:10.1016/j.compositesa.2021.106532.
URL https://linkinghub.elsevier.com/retrieve/pii/S1359835X21002542

[14] C. Yang, X. Tian, D. Li, Y. Cao, F. Zhao, C. Shi, Influence of thermal processing conditions in 3D printing on the crystallinity and mechanical properties of PEEK material, Journal of Materials Processing Technology 248 (2017) 1–7. doi:10.1016/j.jmatprotec.2017.04.027.
URL https://linkinghub.elsevier.com/retrieve/pii/S0924013617301620

[15] D. Yang, Y. Cao, Z. Zhang, Y. Yin, D. Li, Effects of crystallinity control on mechanical properties of 3D-printed short-carbon-fiber-reinforced polyether ether ketone composites, Polymer Testing 97 (2021) 107149. doi:10.1016/j.polymertesting.2021.107149.
URL https://linkinghub.elsevier.com/retrieve/pii/S0142941821000994

[16] S. Berretta, R. Davies, Y. Shyng, Y. Wang, O. Ghita, Fused Deposition Modelling of high temperature polymers: Exploring CNT PEEK composites, Polymer Testing 63 (2017) 251–262. doi:10.1016/j.polymertesting.2017.08.024.
URL https://linkinghub.elsevier.com/retrieve/pii/S014294181730702X

[17] E. Barocio, B. Brenken, A. Favaloro, R. B. Pipes, Interlayer fusion bonding of semi-crystalline polymer composites in extrusion deposition additive manufacturing, Composites Science and Technology (2022) 109334doi:10.1016/j.compscitech.2022.109334.
URL https://linkinghub.elsevier.com/retrieve/pii/S0266353822000768

[18] M. Spoerk, C. Savandaiah, F. Arbeiter, G. Traxler, L. Cardon, C. Holzer, J. Sapkota, Anisotropic properties of oriented short carbon fibre filled polypropylene parts fabricated by extrusion-based additive manufacturing, Composites Part A: Applied Science and Manufacturing 113 (2018) 95–104. doi:10.1016/j.compositesa.2018.06.018.
URL https://linkinghub.elsevier.com/retrieve/pii/S1359835X1830246X

[19] X. Gao, S. Qi, X. Kuang, Y. Su, J. Li, D. Wang, Fused filament fabrication of polymer materials: A review of interlayer bond, Additive Manufacturing 37 (2021) 101658. doi:10.1016/j.addma.2020.101658.
URL https://linkinghub.elsevier.com/retrieve/pii/S2214860420310307

[20] S. Sharafi, M. Santare, J. Gerdes, S. Advani, A review of factors that influence the fracture toughness of extrusion-based additively manufactured polymer and polymer composites, Additive Manufacturing 38 (2021) 101830. doi:10.1016/j.addma.2020.101830.
URL https://linkinghub.elsevier.com/retrieve/pii/S2214860420312021

[21] F. Ning, W. Cong, J. Qiu, J. Wei, S. Wang, Additive manufacturing of carbon fiber reinforced thermoplastic composites using fused deposition modeling, Composites Part B: Engineering 80 (2015) 369–378. doi:10.1016/j.compositesb.2015.06.013.
URL https://linkinghub.elsevier.com/retrieve/pii/S1359836815003777

[22] F. Ning, W. Cong, Y. Hu, H. Wang, Additive manufacturing of carbon fiber-reinforced plastic composites using fused deposition modeling: Effects of process parameters on tensile properties, Journal of Composite Materials 51 (4) (2017) 451–462. doi:10.1177/0021998316646169.
URL http://journals.sagepub.com/doi/10.1177/0021998316646169

[23] G. D. Goh, Y. L. Yap, H. K. J. Tan, S. L. Sing, G. L. Goh, W. Y. Yeong, Process-Structure-Properties in Polymer Additive Manufacturing via Material Extrusion: A Review, Critical Reviews in Solid State and Materials Sciences 45 (2) (2020) 113–133. doi:10.1080/10408436.2018.1549977.
URL https://www.tandfonline.com/doi/full/10.1080/10408436.2018.1549977

[24] M. Gljušcic, M. Franulovic, Žužek Borut, A. Žerovnik, Experimental validation of progressive damage modeling in additively manufactured continuous fiber composites, Composite Structures 295 (2022) 115869. doi:10.1016/j.compstruct.2022.115869.
URL https://linkinghub.elsevier.com/retrieve/pii/S0263822322006365

[25] S. Yu, H. Bale, S. Park, J. Y. Hwang, S. H. Hong, Complex anisotropic fracture behaviors of 3D-printed fiber-reinforced composites based on multi-scale hierarchical microstructure, Composites Science and Technology 218 (2022) 109176. doi:10.1016/j.compscitech.2021.109176.
URL https://linkinghub.elsevier.com/retrieve/pii/S0266353821005327

[26] R. Ghandriz, K. Hart, J. Li, Extended finite element method (XFEM) modeling of fracture in additively manufactured polymers 31 100945. doi:10.1016/j.addma.2019.100945.

URL https://linkinghub.elsevier.com/retrieve/pii/S2214860419305184
[27] D. Yavas, Z. Zhang, Q. Liu, D. Wu, Fracture behavior of 3D printed carbon fiber-reinforced polymer composites, Composites Science and Technology 208 (2021) 108741. doi:10.1016/j.compscitech.2021.108741.
URL https://linkinghub.elsevier.com/retrieve/pii/S026635382100097X
[28] Z. Zhang, D. Yavas, Q. Liu, D. Wu, Effect of build orientation and raster pattern on the fracture behavior of carbon fiber reinforced polymer composites fabricated by additive manufacturing, Additive Manufacturing 47 (2021) 102204. doi:10.1016/j.addma.2021.102204.
URL https://linkinghub.elsevier.com/retrieve/pii/S2214860421003651
[29] M. R. Khosravani, P. Frohn-Srensen, J. Reuter, B. Engel, T. Reinicke, Fracture studies of 3D-printed continuous glass fiber reinforced composites, Theoretical and Applied Fracture Mechanics 119 (2022) 103317. doi:10.1016/j.tafmec.2022.103317.
URL https://linkinghub.elsevier.com/retrieve/pii/S0167844222000696
[30] A. R. Zanjanijam, I. Major, J. G. Lyons, U. Lafont, D. M. Devine, Fused Filament Fabrication of PEEK: A Review of Process-Structure-Property Relationships, Polymers 12 (8) (2020) 1665. doi:10.3390/polym12081665.
URL https://www.mdpi.com/2073-4360/12/8/1665
[31] J. Pu, C. McIlroy, A. Jones, I. Ashcroft, Understanding mechanical properties in fused filament fabrication of polyether ether ketone, Additive Manufacturing 37 (2021) 101673. doi:10.1016/j.addma.2020.101673.
URL https://linkinghub.elsevier.com/retrieve/pii/S2214860420310459
[32] B. Brenken, E. Barocio, A. Favaloro, V. Kunc, R. B. Pipes, Fused filament fabrication of fiber-reinforced polymers: A review, Additive Manufacturing 21 (2018) 1–16. doi:10.1016/j.addma.2018.01.002.
URL https://linkinghub.elsevier.com/retrieve/pii/S2214860417304475
[33] D. Yavas, Z. Zhang, Q. Liu, D. Wu, Interlaminar shear behavior of continuous and short carbon fiber reinforced polymer composites fabricated by additive manufacturing, Composites Part B: Engineering 204 (2021) 108460. doi:10.1016/j.compositesb.2020.108460.
URL https://linkinghub.elsevier.com/retrieve/pii/S1359836820335095
[34] Tecapeek cf30 black, Tech. rep., Ensinger.
URL https://www.ensingerplastics.com/en/shapes/products/peek-tecapeek-cf30-black
[35] D20 Committee, Test Methods for Plane-Strain Fracture Toughness and Strain Energy Release Rate of Plastic Materials, Tech. rep., ASTM International. doi:10.1520/D5045-14.
URL http://www.astm.org/cgi-bin/resolver.cgi?D5045-14
[36] D20 Committee, Test Method for Tensile Properties of Plastics, Tech. rep., ASTM International. doi:10.1520/D0638-14.
URL http://www.astm.org/cgi-bin/resolver.cgi?D638-14
[37] A. Lingua, N. Piccirelli, D. Therriault, M. Lévesque, In-situ full-field measurements for 3d printed polymers during mode i interface failure, Engineering Fracture Mechanics 269 (2022) 108483. doi:https://doi.org/10.1016/j.engfracmech.2022.108483.
URL https://www.sciencedirect.com/science/article/pii/S0013794422002260
[38] Correlated s. vic-3d help manual, Tech. rep., Correlated Solutions.
URL http://www.correlatedsolutions.com/installs/Vic-3D-2010-manual.pdf
[39] I. Tabiai, G. Tkachev, P. Diehl, S. Frey, T. Ertl, D. Therriault, M. Lévesque, Hybrid image processing approach for autonomous crack area detection and tracking using local digital image correlation results applied to single-fiber interfacial debonding 216 106485. doi:10.1016/j.engfracmech.2019.106485.
URL https://linkinghub.elsevier.com/retrieve/pii/S0013794418312530
[40] F. Sosa-Rey, Y. Abderrafai, A. Diouf Lewis, D. Therriault, N. Piccirelli, M. Lévesque, OpenFiberSeg: Open-source segmentation of individual fibers and porosity in tomographic scans of additively manufactured short fiber reinforced composites, Composites Science and Technology 226 (2022) 109497. doi:10.1016/j.compscitech.2022.109497.
URL https://linkinghub.elsevier.com/retrieve/pii/S0266353822002391

[41] R. T. L. Ferreira, I. C. Amatte, T. A. Dutra, D. Bürger, Experimental characterization and micrography of 3D printed PLA and PLA reinforced with short carbon fibers, Composites Part B: Engineering 124 (2017) 88–100. doi:10.1016/j.compositesb.2017.05.013.
URL https://linkinghub.elsevier.com/retrieve/pii/S135983681633195X

[42] F. Sosa-Rey, C. Vella, A. Lingua, J. Pierre, N. Piccirelli, D. Therriault, L. Martin, Multiscale fast fourier transform homogenization of additively manufactured fiber reinforced composites from component-wise description of morphology, submitted to Composites Science and Technology (Jan. 2023).

[43] A. Abbott, G. Tandon, R. Bradford, H. Koerner, J. Baur, Process-structure-property effects on ABS bond strength in fused filament fabrication, Additive Manufacturing 19 (2018) 29–38. doi:10.1016/j.addma.2017.11.002.
URL https://linkinghub.elsevier.com/retrieve/pii/S2214860417300933